Nonaxisymmetric simulations of the Princeton magnetorotational instability experiment with insulating and conducting axial boundaries

Dahan Choi,[1] Fatima Ebrahimi,[1,2] Kyle J. Caspary,[2] Erik P. Gilson,[2] Jeremy Goodman,[1] and Hantao Ji[1,2]
[1]*Department of Astrophysical Sciences, Princeton University, Princeton, NJ 08544, USA*
[2]*Princeton Plasma Physics Laboratory, Princeton University, Princeton, NJ 08543, USA*

(Received 21 December 2018; published 24 September 2019)

Stability and nonlinear evolution of rotating magnetohydrodynamic flows in the Princeton magnetorotational instability (MRI) experiment are examined using three-dimensional non-axisymmetric simulations. In particular, the effect of axial boundary conductivity on a free Stewartson-Shercliff layer (SSL) is numerically investigated using the spectral finite-element Maxwell and Navier Stokes (SFEMaNS) code. The free SSL is established by a sufficiently strong magnetic field imposed axially across the differentially rotating fluid with two rotating rings enforcing the boundary conditions. Numerical simulations show that the response of the bulk fluid flow is vastly different in the two different cases of insulating and conducting end caps. We find that, for the insulating end caps, there is a transition from stability to instability of a Kelvin-Helmholtz-like mode that saturates at an azimuthal mode number $m = 1$, whereas for the conducting end caps, the reinforced coupling between the magnetic field and the bulk fluid generates a strong radially localized shear in the azimuthal velocity resulting in axisymmetric Rayleigh-like modes even at reduced thresholds for the axial magnetic field. For reference, three-dimensional nonaxisymmetric simulations have also been performed in the MRI unstable regime to compare the modal structures.

DOI: 10.1103/PhysRevE.100.033116

I. INTRODUCTION

Angular momentum transport in accretion disks has been of great interest as the gravitationally contracting material must transport angular momentum outward through means of instabilities and turbulence [1–3]. Because the specific angular momentum (Ωr^2), Ω being angular speed and r being radius, for these accretion disks undergoing Keplerian motion increases radially outward, accretion disks are hydrodynamically stable to Rayleigh's centrifugal instability. Although nonlinear hydrodynamic instabilities also might arise in such systems, experimental and numerical work suggest that such accretion disks are stable against purely hydrodynamic modes [4–7], in particular, in the absence of special features [8] and some physical stratifications [9,10]. Therefore, the magnetorotational instability (MRI) [11,12], the magnetohydrodynamic (MHD) instability of a differentially rotating flow in the presence of a weak magnetic field, is believed to be the driving mechanism of angular momentum transport in astronomical accretion disks [3].

In search of MRI in the laboratory, experiments have been dedicated to studying the stability of differentially rotating flows in the MHD regime. Global MHD simulations are also critical to investigate the onset and saturation of MRI in Taylor-Couette flow geometry [13–18] or in plasma [19] experiments. In particular, in order to understand the liquid-boundary interactions of the experimental apparatus, global simulations with realistic boundary conditions are crucial. In this paper, using global MHD simulations, we investigate the effect of experimental axial boundaries in the Princeton MRI experiment. The Princeton MRI experiment has been developed to demonstrate MRI in a laboratory setting using a magnetized conducting fluid (GaInSn) rotating in a modified Taylor-Couette device [20,21].

In Taylor-Couette devices, there are hydrodynamic boundary layers that form due to differences in the rotation rate between the boundaries and interior (bulk) fluid, such as Ekman layers and Stewartson layers forming perpendicular and parallel to the rotation axis [22,23]. These boundary layers drive nontrivial secondary circulation that modifies the bulk flow profile as a whole. The strengths of these circulations are determined by the differential rotation rates of the Taylor-Couette device. On the other hand, there are magnetic-liquid interactions that arise when an axial magnetic field is applied across the system to drive MRI, such as magnetized Ekman or Hartmann and magnetized Stewartson or Shercliff layers (SSLs) that form perpendicular and parallel to the background field [24,25] in addition to MRI. Furthermore, induced current loops that close around these layers can also nontrivially affect the background flow dynamics with the strength of these interactions determined by the fluid-boundary conductivities.

Understanding these secondary circulations is of great importance for identifying MRI in a laboratory setting. Initial experimental and computational studies [26,27] were conducted with insulating boundaries; however, recent computational work has been carried out motivated by the change from insulating axial boundary end caps to conducting ones. Wei *et al.* [28] discovered that changes in the radial magnetic field corresponded well to the previously calculated MRI thresholds and that the nonlinear saturation of the root mean

square of the total (volume averaged) radial magnetic field (the "MRI signal") had similar dependence on key parameters, such as the background magnetic field, as the linear MRI growth rate. Most importantly, the simulations showed that the MRI signal with conducting axial boundaries is significantly increased [28] from the MRI signal with insulating axial boundaries. Based on these numerical predictions, the axial boundaries have been changed to copper in the present Princeton MRI experiment. Experimental studies have been recently conducted in the slow-rotation regime to understand the fluid response under the new boundary conditions [29], revealing a vastly different instability response in the two cases. Developing a thorough understanding of the full fluid response in this slow-rotation regime is essential for providing guidance for planned experiments as well as numerical calculations in the experimentally relevant fast-rotating MRI-unstable regime. Similar experimental and numerical studies [30,31] have been conducted comparing insulating and conducting axial boundaries to understand the effects of boundary layers on the evolution of helical MRI in the Potsdam Rossendorf magnetic instability experiment and have led to an improved characterization of helical MRI [32].

In this paper, we utilize three-dimensional (3D) nonaxisymmetric calculations to study numerically the formation of SSLs, the resulting mode structures, and mechanism of the instabilities. We first perform simulations with the initial flow and parameter space as close as possible to the actual experiments [29] for direct comparisons. Consistent with the experimental results [29], numerical MHD simulations using the spectral finite-element Maxwell and Navier-Stokes solver (SFEMaNS) [33] code show that the response of the bulk fluid flow is also vastly different in the two different cases of insulating and conducting end caps. We find that, for the insulating end caps, there is a transition from stability to instability of a Kelvin-Helmholtz-like (K-H) mode that saturates at an azimuthal mode number of $m = 1$, whereas for the conducting end caps, the reinforced coupling between the magnetic field and the bulk fluid generates a strong shear in the azimuthal velocity resulting in axisymmetric Rayleigh-like modes (with hydrodynamic instability criterion for the angular momentum $\partial L/\partial r < 0$) at reduced thresholds for the axial magnetic field. Good agreement between the simulations and the experimental results are obtained; for the insulating boundary experiments, there is a coherent $m = 1$ instability that develops in the azimuthal flow, and for the conducting boundary experiments, a strong shear profile similar to the numerical predictions is seen. We further compare the resulting mode structure of the Rayleigh-like modes in the conducting boundary simulations with the MRI mode structures in a reference simulation case.

The paper is organized as follows. The simulation method and its experimental relevance are discussed in Sec. II. In Sec. III, we present energy and eigenstructure analysis for insulating and conducting boundary conditions as well as comparisons with a reference MRI unstable case. We summarize the results in Sec. IV and present implications for future simulations and experimental efforts to identifying MRI in the Princeton MRI experiment.

II. METHODS

Nonaxisymmetric 3D numerical simulations were conducted with the SFEMaNS [33]. The solver uses a Fourier spectral method in azimuth and a finite-element method in the meridional plane with up to 72 000 triangular finite-element slices. Although previous work [28] focused on axisymmetric perturbations (with only the $m = 0$ mode fully resolved), up to 16 spectral azimuthal modes are resolved here to search for nonaxisymmetric shearing layer instabilities. Each instance of the 3D nonaxisymmetric simulation uses 256 cores running in parallel with 2 GB memory per core and requires 3 weeks to complete.

We solve the dimensionless Navier Stokes equation in the fluid domain modeled for the Princeton MRI experiment using a cylindrical coordinate system with the units of length, time, magnetic field, and conductivity being r_1, Ω_1^{-1}, $r_1\Omega_1\sqrt{\rho\mu_0}$, and σ with ρ and σ representing the density and conductivity. The dimensionless parameters of the system are the fluid Reynolds number $\mathrm{Re} \equiv \Omega_1 r_1^2/\nu$ corresponding to the viscosity, the magnetic Reynolds number $\mathrm{Rm} \equiv \Omega_1 r_1^2 \sigma_{\mathrm{GaInSn}}\mu_0$ determining the rotation rate, the Lehnert number $B_0 \equiv V_A/\Omega_1 r_1$ corresponding to the magnetic field strength with $V_A \equiv B/\sqrt{\mu_0\rho}$ the Alfvén velocity, and the Elsasser number $\Lambda \equiv B_0^2\mathrm{Rm}$ which is the ratio of the Lorentz and Coriolis forces.

Figure 1 shows the simulation domain. The fluid is encapsulated in four rotating parts: the inner cylinder, inner ring, the outer cylinder, and the outer ring. The radii of the inner and outer cylinders are $r_1 = 7$ and $r_2 = 21$ cm, respectively; the end caps are divided into differentially rotating inner and outer rings to suppress secondary circulations [34]. The transition radius between inner and outer rings is $r_t = 14$ cm, and the height of the fluid domain is $h = 28$ cm. The end cap thickness $d = 2$ cm determines the effective electrical thickness $\delta \equiv \sigma_{\mathrm{Cu}} d/\sigma_{\mathrm{GaInSn}}$. The induction equation is solved

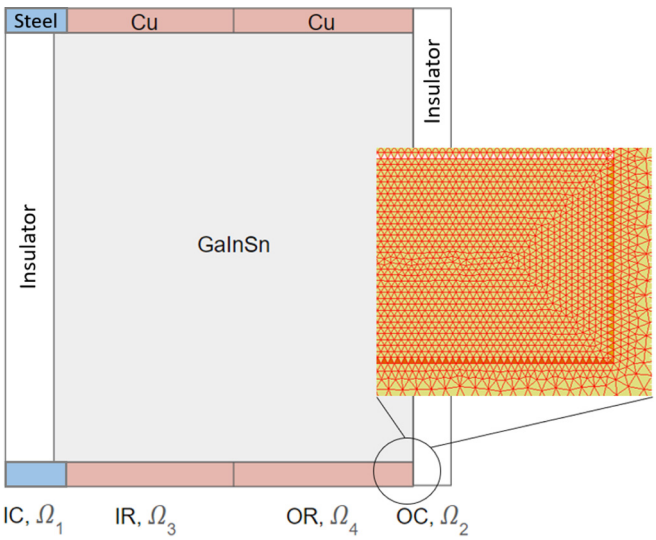

FIG. 1. Initialization of the simulation domain. The inner cylinder is composed of an insulating shell with stainless steel ends, and the outer cylinder is composed of stainless steel in the experiments and an insulator in the simulations. The inner and outer rings are composed of copper. The working fluid is GaInSn.

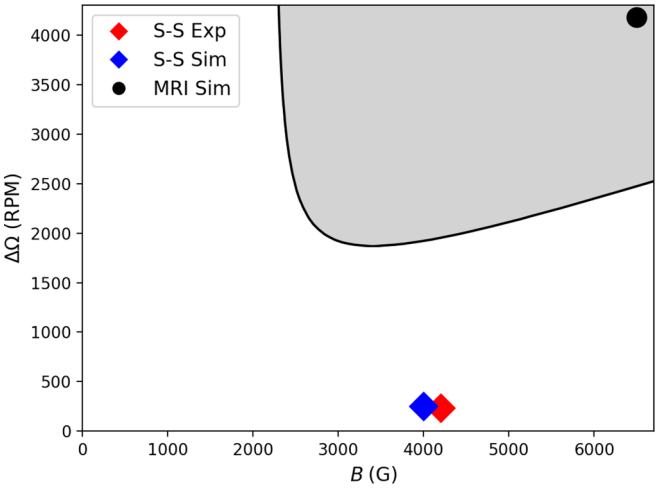

FIG. 2. Visualization of the parameter space involved in the simulations and experiments with the curve representing marginal stability and the shaded area representing the MRI unstable regime. The red and blue diamonds, respectively, represent the split-stable experiment and simulations that were conducted in the slow-rotation regime. The black dot represents the MRI simulation in the fast-rotation regime with the background field $B = 6500$ G and the differential rotation rate $\Delta\Omega = \Omega_1 - \Omega_2 = 4250$ rpm.

in the fluid and solid domains, namely, the conducting fluid, the copper end caps, and the steel inner cylinder ends. Finally, a spherical vacuum domain with radius $r_s = 280$ cm surrounds the fluid and solid domains. For the insulating end cap simulations, the induction equation is no longer solved in the solid domain, and the entirety of the solid domain is incorporated into the vacuum domain, representing full insulating axial boundaries in the experiment.

We primarily perform our analysis under two different regimes of rotation rates: the slow rotation rate (Rm ~ 0.6) with the split-stable (S-S) rotation profile devised to visualize the hydrodynamic response and compare with initial experimental results [29], and the fast rotation rate (Rm ~ 10) with the MRI rotation profile to highlight the differences in mode structure between the slowly rotating magnetohydrodynamic response and the fast rotating MRI. In the stability diagram in Fig. 2, the red and blue diamonds represent the experimental and simulational parameters for the slow rotation regime, respectively, and the black dot represents the simulation parameters for the fast rotation regime. The axial field values B were chosen to amplify the fluid response in the slow rotation regime and to fully destabilize MRI in the fast rotation regime.

A S-S rotation profile composed of corotating inner and outer components, respectively, is enforced in the simulations to amplify the effects of the shear inside the fluid domain. The inner cylinder, inner ring, outer ring, outer cylinder rotations Ω_1, Ω_3, Ω_4, and Ω_2 were configured at the relative rates $\Omega_1 = \Omega_3$, $\Omega_2 = \Omega_4 = 0.25\Omega_1$ ($\Omega_1 = 335$ rpm) for this setup with no-slip boundary conditions between the ring-fluid interface. The initial bulk fluid rotations were matched to the respective ring rotations piecewise uniformly and relaxed until a hydrodynamically steady rotation profile was established to closely emulate the real experimental rotation profile. Figure 3 shows this initial background rotation profile Ω as a function

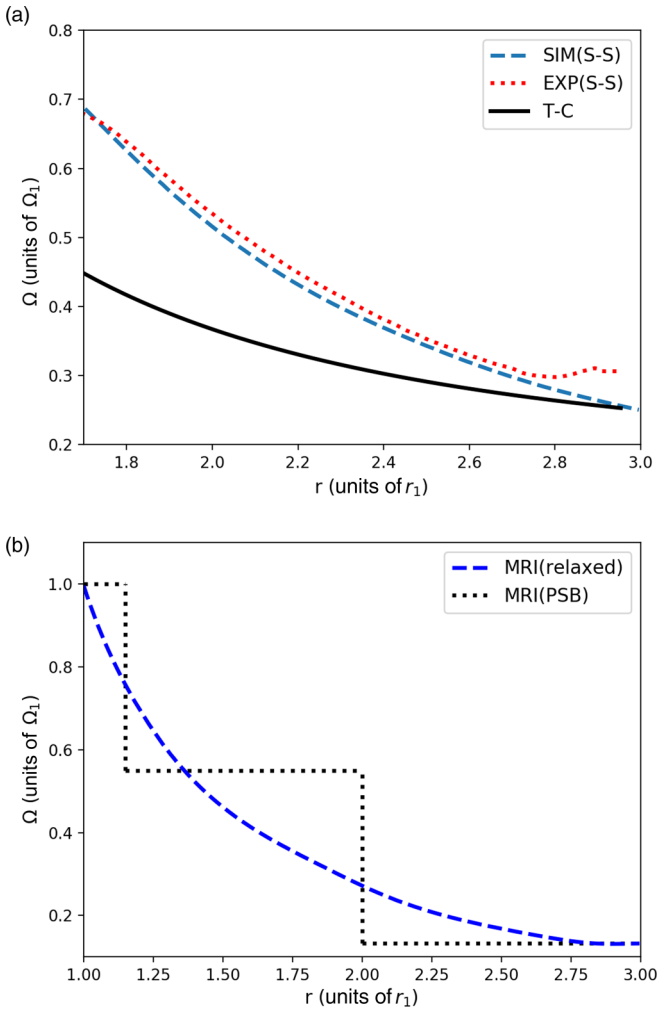

FIG. 3. Plots of the fluid rotation rate Ω as a function of radius taken at the midplane ($z = 0$) of the system. (a) Initialization of the hydrodynamically stable initial state is performed by relaxing a piecewise uniform state matched at the rotation rates of the boundaries to more precisely emulate real experimental fluid flows. The simulation flow for the split-stable case is indicated by a dashed blue line, the experimental flow by a dotted red line, and the ideal Taylor-Couette solution by a solid black line. The experimental flow is collected using ultrasound Doppler velocimetry from a run with the same ratio of inner and outer components but at a slightly higher rotation rate. (b) Reference MRI unstable case with piecewise solid body (PSB) initial state and the relaxed rotation profile. The relaxed rotation profile is the effective initial state, which could trigger MRI for this reference case.

of radius r at the midplane; although there are some slight discrepancies in the flow between $r = 1.25$ and $r = 1.75$, overall the experimental and simulated flow closely resemble each other in the bulk fluid. The initial flow for the simulations failed to be hydrodynamically stable for Rossby number $\mathrm{Ro} \equiv (\Omega_1 - \Omega_2)/\Omega_2 = 2.35$ matching the experiment, so a higher differential rotation rate with $\mathrm{Ro} = 3$ was used to develop the hydrodynamically stable initial flow in the simulations [35].

For reference, we have also performed 3D nonaxisymmetric simulations of the MRI unstable case with the MRI rotation profile that leads to the optimization of the MRI

TABLE I. Experimental parameters of the physical system are displayed. The physical dimensions of the experimental apparatus, the differential rotation rates, the densities of the end caps, working fluid, and the conductivities are summarized.

Experimental parameters Split-Stable experiment	
r_1	6.9 cm
r_2	20.3 cm
r_t	13.5 cm
h	28 cm
d	2 cm
Ω_1, Ω_3	335 rpm
Ω_2, Ω_4	100 rpm
ρ_{Cu}	9.0 g/cm^3
ρ_{GaInSn}	6.3 g/cm^3
σ_{Cu}	6.0×10^7 $(\Omega\,\mathrm{m})^{-1}$
σ_{GaInSn}	3.5×10^6 $(\Omega\,\mathrm{m})^{-1}$
σ_{steel}	1.75×10^6 $(\Omega\,\mathrm{m})^{-1}$
B	4200 G

signal [28]. The relative rotation rates were configured at $\Omega_3 = 0.55\Omega_1$, $\Omega_4 = \Omega_2 = 0.1325\Omega_1$ ($\Omega_1 = 5000$ rpm), and the background magnetic field $B_0 = 0.2$ ($B = 6500$ G). This simulation is not exactly experimentally relevant as the background magnetic field is initialized instantaneously after the piecewise solid body initial state is enforced where the fluid in the entire volume has the same velocity as the rotating boundaries. However, the flow responds to the applied field and relaxes rapidly before MRI growth so that the relaxed flow could be considered as the effective initial state. Figure 3(b) shows the rotation profiles of the piecewise solid body initial state and the relaxed flow immediately after magnetic field application.

Table I lists the experimental parameters used in the split-stable experiments [29]. The experimental parameters are normalized to the aforementioned scaling in the simulations. The dimensionless constants of the simulations and experiments are summarized in Table II. The dimensionless constants for the split-stable simulations and experiments are relatively similar with the exception of the fluid Reynolds number, which is Re $\sim 10^6$ in the experiments but is Re $= 1000$ in the simulations due to computational limitations.

TABLE II. Dimensionless parameters of the system are displayed. The dimensionless parameters are the fluid Reynolds number, the magnetic Reynolds number, the axial magnetic field strength, and the Elsasser number which corresponds to the viscosity of the system, the rotation rate, the background magnetic field, and the relative strength of the Lorentz force and Coriolis force, respectively.

Experiment Split stable		Simulation Split stable		Simulation MRI	
Re	10^6	Re	1000	Re	1000
Rm	0.68	Rm	0.68	Rm	10
B_0	1.89	B_0	1.8	B_0	0.2
Λ	2.44	Λ	2.21	Λ	0.4

III. SIMULATION RESULTS

Here, we present simulation results for the two cases of the S-S case and the MRI unstable case. In the split-stable configuration, the inner and outer cylinders rotate with the inner and outer rings, respectively, relaxing to a flow with larger shear around the midradius. The effect of insulating and conducting end cap boundaries are presented for this case. For the reference unstable MRI case, a piecewise solid body initial state (with three rotational frequencies) relaxes to a state with lower flow shear unstable to MRI. For the conducting end cap cases, the resulting mode structures and energies for the S-S case are compared with the MRI case.

A. Split-stable case

Previous experimental results show that, for insulating end caps, an instability with azimuthal mode number $m = 1$ develops, caused by the formation of magnetized SSLs driven by the background axial field above the threshold $\Lambda_{\mathrm{Ga}} > 1$ [27,29]. The results from the nonaxisymmetric simulations show the same general trend; after the background axial field is applied, the azimuthal velocity becomes globally destabilized by the formation of free SSLs near the inner and outer ring boundaries. These fluctuations culminate in Kelvin-Helmholtz-like modes with an axially uniform structure and azimuthal mode structure transitioning from $m = 4$ to $m = 1$.

In Fig. 4, we see the volumetrically averaged kinetic energy of the insulating end cap system without the background mean flow contribution. There is a modal cascade of power from $m = 4$ to $m = 1$ in the kinetic energy spectrum of the system with the $m = 1$ contribution exponentially growing at early times. This qualitatively agrees well with the previous results with the emergence of a single dominant mode from initial multiple mode spectra [27,29]. The nonaxisymmetric

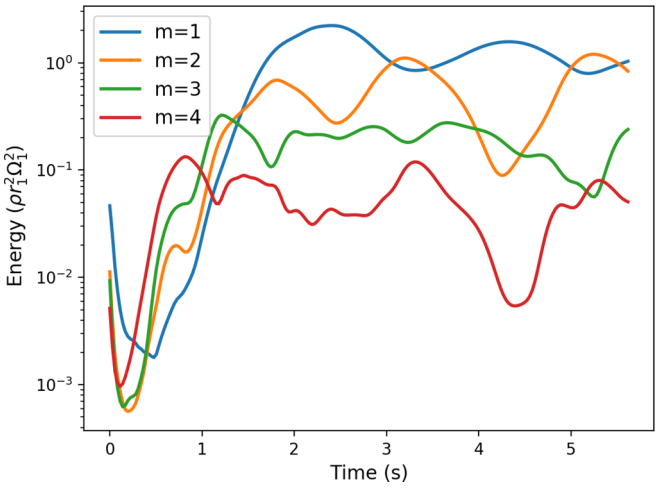

FIG. 4. Calculated volumetrically averaged kinetic energy contributions for the S-S insulating boundary simulations from azimuthal modes $m = 1$ to $m = 4$. Higher azimuthal modes are not active.

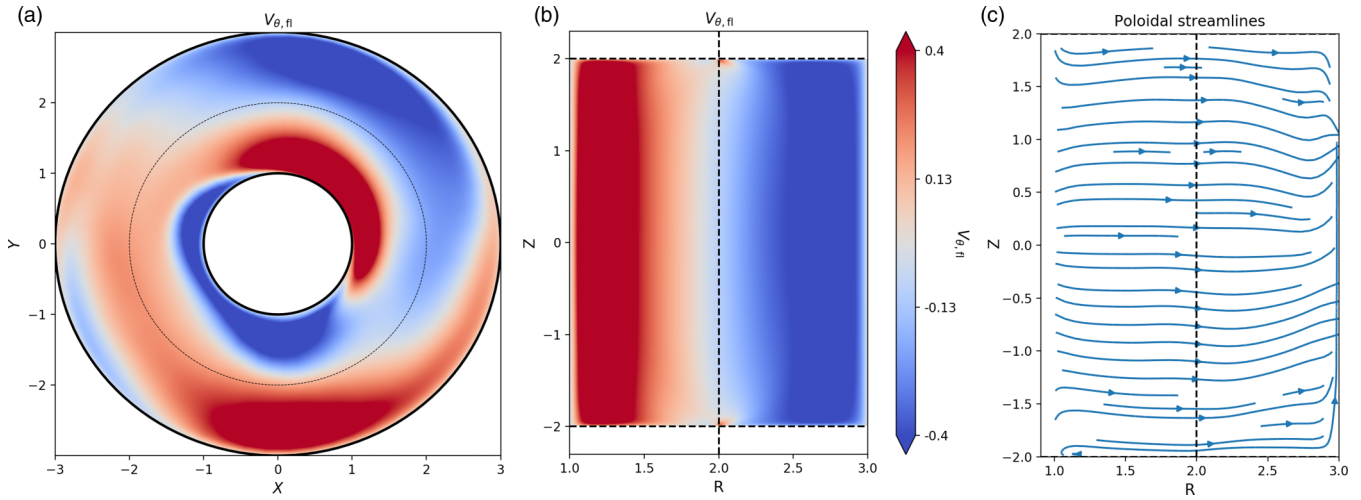

FIG. 5. The mode structures of the split-stable insulating simulation calculated for the normalized fluctuating azimuthal velocity $V_{\theta,\mathrm{fl}} = (V_\theta - V_{\mathrm{mean}})/V_{\mathrm{mean}}$. (a) shows the azimuthal mode structure at the midplane ($z = 0$), and (b) shows the axial (r-z) mode structure and streamlines at the azimuthal cross section $\theta = \pi/2$, (c) shows poloidal streamlines. The computational data were taken at $t = 2.1$ s when the $m = 1$ contribution was dominant.

contribution to the volumetric kinetic energy is resolved fully; kinetic energies from higher mode numbers $m > 4$ are orders of magnitude less than those from $m \leqslant 4$ and do not contribute significantly to the volumetrically averaged kinetic energy.

Fluctuating azimuthal velocities $V_{\theta,\mathrm{fl}}$ were calculated by subtracting the time averaged mean flow V_{mean} from V_θ and plotted onto horizontal and vertical planes. The mode structures depicted in Fig. 5 clearly show the dominant $m = 1$ instability in the horizontal cross section at the midplane, indicating that the magnetized SSL produced a global instability throughout the bulk fluid rather than localized behavior near the end caps. The instability also has an axially uniform profile.

In contrast to the gradual and coherent fluid response under insulating end caps, the fluid response is much more dynamic and rapid when conducting boundaries are enforced. A comparison between the azimuthal velocities of the insulating and conducting end caps after the background magnetic field is applied shows that there is an immediate response in the conducting case that leads to changes in the mean fluid flow and changes to the structural complexity of the azimuthal velocity fluctuations, whereas, in the insulating case, the fluctuations develop more gradually and are more structured. The $m = 1$ mode eventually dominates in the insulating case, but plots of the modal structure of the conducting case show that after the initial change in mean flow the fluctuations maintain an apparent azimuthal structure of $m = 2$.

The volumetrically averaged kinetic energy graph is shown in Fig. 6 for the conducting boundaries. Comparing to the insulating case, the onset of instabilities in the conducting boundaries case is much more rapid and diverse. Although the strength of the modal fluctuations is weaker at a normalized value of 0.1–0.2, there is no single mode that contributes dominantly to the kinetic energy; rather, multiple high-frequency modes contribute. However, the primary difference lies in the $m = 0$ axisymmetric evolution. In the conducting case, we see an immediate increase in the $m = 0$ kinetic energy which translates to a sudden change in the mean flow of the system compared to the insulating case where the mean flow does not change drastically. The inset in Fig. 6(b) shows the change in the bulk flow as the $m = 0$ growth sets in; the strong shear is rapidly established as the total energy in the bulk flow is established.

Because the azimuthal velocity V_θ includes the $m = 0$ background mean flow, the radial (V_r) and axial (V_z) velocity perturbations were visualized instead to look at the mode structure of the instabilities. Figure 7 shows the azimuthal and axial mode structures of the instability. There is a clear $m = 0$ structure in both the radial and the axial components of velocity. There seems to also be some modal breakdown into a higher frequency in localized parts of the system near the axial boundaries, indicating that the system is evolving quickly and transitioning from the linear phase to the turbulent phase. The axial cross sections show coherent structures on the meridional plane; most noticeably, we have four circulatory cells that span the axial plane when the instability is saturated. The drastically different mode structure for the conducting boundaries suggests a completely different instability response mechanism compared to the insulating boundaries. For the insulating boundaries, the instability culminated in K-H-like modes with $m = 1$ and the axially uniform mode structure, whereas for the conducting boundaries the resulting instability was an axisymmetric $m = 0$ mode with circulating cells on the meridional plane hinting at Rayleigh-like modes.

To investigate the difference between the conducting and the insulating response, the current response to the background axial magnetic field is plotted in Fig. 8. Almost immediately after the background magnetic field is turned on, large currents develop in the end cap boundaries for the conducting case. These thick boundary layer currents and the high conductivity of the end caps lead to strong magnetic coupling of the fluid to the boundaries and result in significant return currents in the fluid volume itself. The large return currents ultimately drive strong azimuthal Lorentz forces and Maxwell stresses that reinforce the fluid rotation in the inner fluid volume whereas decreasing the rotation of the outer fluid

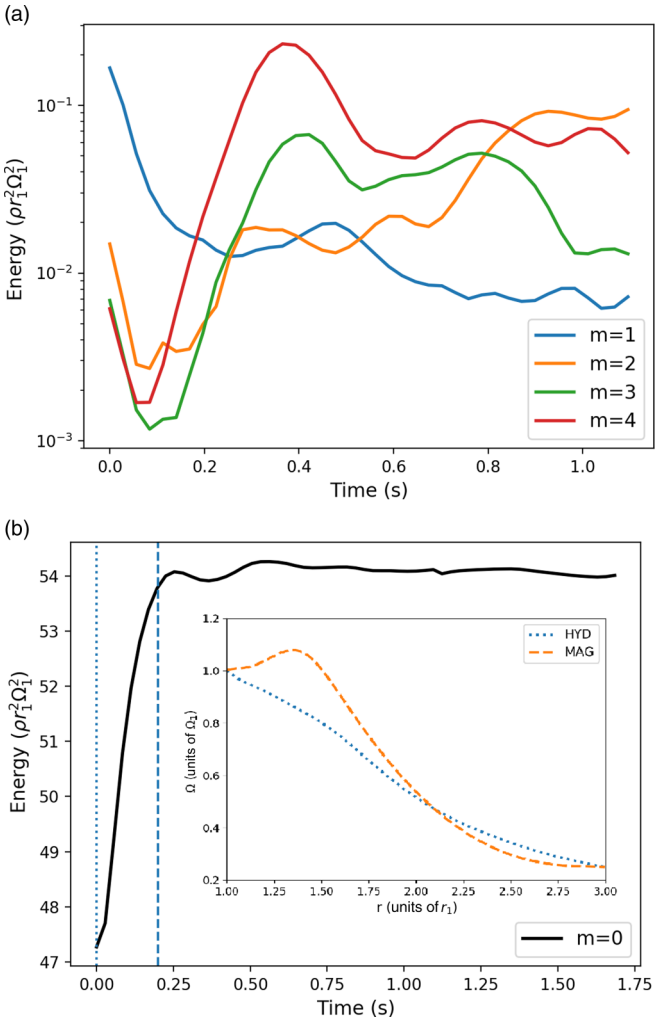

FIG. 6. Calculated volumetrically averaged kinetic energy contributions for conducting boundary S-S simulations. (a) Azimuthal modes $m = 1$ to $m = 4$, and (b) $m = 0$, and the inset shows the flow profile before initialization and after the $m = 0$ mode growth. Higher azimuthal modes are not active.

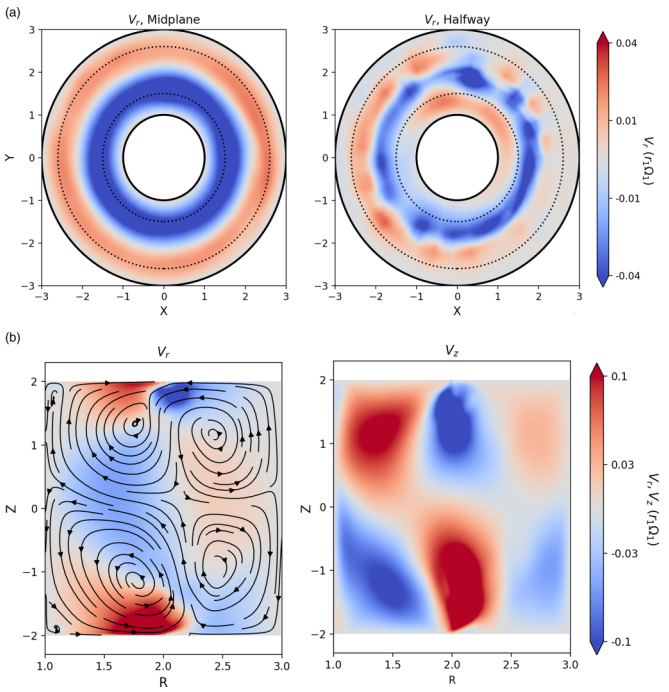

FIG. 7. The mode structures of the S-S conducting simulation calculated for the fluctuating radial and axial velocity V_r, V_z. (a) shows the azimuthal mode structure of V_r at the midplane ($z = 0$) and halfway to the axial boundaries ($z = 1$), and (b) shows the axial mode structures of V_r, V_z and streamlines at the azimuthal cross section $\theta = \pi/2$. The data were taken at $t = 0.1$ s when the $m = 0$ contribution was growing rapidly.

volume, resulting in a sharp shear that drives the system to a Rayleigh unstable state. In contrast, this effect is not observed in the insulating case where the end caps are treated as part of the vacuum; a small volume of fluid along the boundary interface forms a thin layer on the fluid-vacuum interface, effectively taking the place of the conducting end caps. However, the low conductivity and small current layer thickness result in a much weaker coupling between the boundary and the fluid compared to fully conducting boundaries. This culminates as minimal return currents that do not significantly increase the flow shear of the system and remains stable to Rayleigh instabilities whereas still unstable to the magnetic Kelvin-Helmholtz instability for the insulating boundaries as reported previously [26,27].

The effect of the Lorentz forces on the hydrodynamic stability of the system in both the conducting and the insulating cases can be seen in Fig. 9 where the shear profile $q = -\partial \ln \Omega/\partial \ln r$ at various times are plotted. Almost immediately after application of the background field ($t = 0.1$ s), a localized peak that is above the Rayleigh stability threshold of $q = 2$ appears in the shear profile for the conducting boundaries, whereas the shear profile for the insulating boundaries remains relatively unchanged. This leads to an immediate growth in the Rayleigh-like structures shown in Fig. 7 for the conducting case. For the insulating case, the development of shear is very slow; the shear eventually does go above the

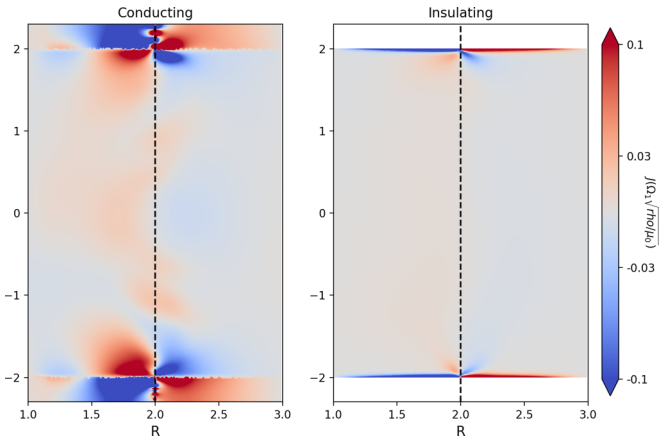

FIG. 8. The current responses J_r to the background magnetic field for the S-S conducting and insulating simulations. The current response and resulting Lorentz forces are strong and immediate for conducting case whereas the current response is weak for the insulating case.

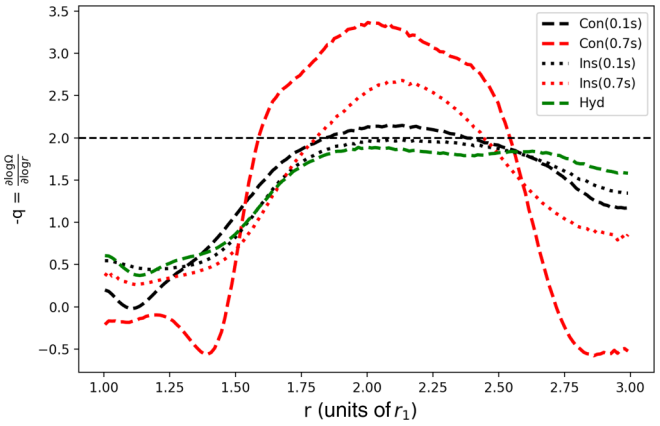

FIG. 9. $q = -\partial \ln \Omega/\partial \ln r$ plots at times $t = 0.1$ s colored in black and $t = 0.7$ s colored in red, taken at the midplane for the S-S simulations. The hydrodynamically stable initial state is colored in green. Early time behavior suggests that the response of the shear is rapid in the conducting case, whereas it is slower for the insulating case. Later time behavior has the shear above the Rayleigh threshold $q = 2$ for both the conducting and the insulating cases, but the increased shear is maintained in the conducting case whereas it is flattened for the insulating case as the K-H mode develops.

Rayleigh unstable limit at later times ($t = 0.7$ s), but the onset of K-H modes forces the shear profile back below the $q = 2$ threshold.

The late time shear profiles for the simulations and experiments are plotted in Fig. 10. The shear in the insulating end cap simulations stays below $q = 2$ after the development of the K-H-like mode except at the inner and outer cylinder boundaries where viscous forces play a large role. The shear in the conducting simulations shows localization of the shear above the Rayleigh stability threshold $q = 2$ between the radii

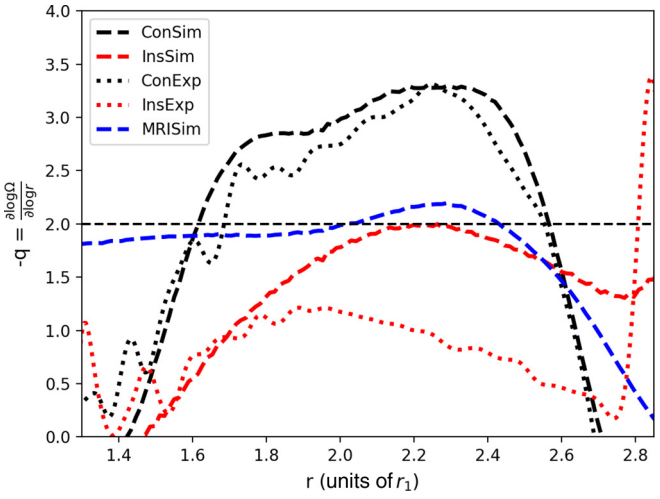

FIG. 10. $q = -\partial \ln \Omega/\partial \ln r$ plots versus radius at late times, taken at the midplane for the S-S simulations and experiments. q values above 2 are linearly unstable to Rayleigh's centrifugal instability. The black line indicates the q profile of the conducting end caps, whereas the red line indicates the q profile of the insulating end caps. The blue line indicates the q profile of the MRI unstable configuration with conducting end caps.

$r = 1.6$ and $r = 2.5$. Referring back to Fig. 7, we observe that the conducting $m = 0$ mode structure is also localized around these radii where $q > 2$, indicated in light dashed lines, supporting the onset of hydrodynamically unstable Rayleigh modes. Experimentally, similar q profiles are seen in the conducting case; the same large shear is established between $r = 1.6$ and $r = 2.5$. In the insulating case, the shear also stays well below $q < 2$, but the shear profile deviates from the numerical values. This is probably because viscous forces are nontrivial in the insulating case and the computational restraints on fluid Reynolds number, which is $1/1000$ that of the experiment, impact the flow dynamics.

The difference in response for the conducting and insulating boundaries can be understood through the work performed on line-tied K-H instabilities by Miura and Kan [36]. Although the stability analysis performed by Miura and Kan is for an infinite slab geometry with vertical boundaries of finite thickness and conductivity, a rough estimate for the stability of the cylindrical system can be extrapolated by transforming the longitudinal coordinate to the azimuthal coordinate. Modifying Eq. (36) in this paper for our cylindrical system gives the linear growth rate γ of line-tied K-H modes for finite axial wave numbers,

$$\gamma^2 = m^2(V_\theta/r_1)^2 - k_z^2 V_A^2. \tag{1}$$

Using the values of $m = 1$, $V_\theta/r_1 = 33.5$ rad/s, $k_z = \pi/28$ cm, and $V_A = 4.5$ m/s, the growth rate γ^2 is negative, indicating that the K-H mode is stabilized in the conducting boundary system. Note that we have used the longest axial wavelength due to the line-tied boundary condition. The mode structures with nonzero k_z that are demanded by the line-tied conducting axial boundaries contribute to magnetic field bending and stabilize the K-H modes.

However, in the insulating case, the most unstable K-H mode is associated with $k_z \sim 0$ resulting in the linear growth rate in Eq. (40) of Ref. [36],

$$\gamma = -\mu_0(\sigma_{\mathrm{GaInSn}} d)V_A^2/h + \left\{\left[\mu_0(\sigma_{\mathrm{GaInSn}} d)V_A^2/h\right]^2 + m^2(V_\theta/r_1)^2\right\}^{1/2}. \tag{2}$$

Using the values of m, V_θ/r_1, and V_A listed above, the conductivity of the fluid layer $\sigma_{\mathrm{GaInSn}} = 3.5 \times 10^6\ (\Omega\,\mathrm{m})^{-1}$ and the value of $d = 0.14$ cm as a rough estimate of the layer width using the current profiles in Fig. 8, the theoretical growth rate is $\gamma_{\mathrm{th}} = 33.1\ \mathrm{s}^{-1}$. Analyzing the growth rate of the line-tied K-H instability in the insulating simulations from Fig. 4 gives the numerical growth rate $\gamma_{\mathrm{sim}} = 4.8\ \mathrm{s}^{-1}$. Despite the differences in the initial configuration (slab versus cylindrical) and instability stage (local linear theory versus global nonlinear simulations), the linear theory presented by Miura and Kan qualitatively agrees with the results of the simulations, predicting suppression of line-tied K-H modes in the conducting case and the growth of said modes in the insulating case. Modification of the line-tied K-H theory for the cylindrical geometry in the MRI experiments remains for future work.

B. Reference MRI unstable case

Three-dimensional nonaxisymmetric simulations of the MRI unstable configuration with conducting boundaries are

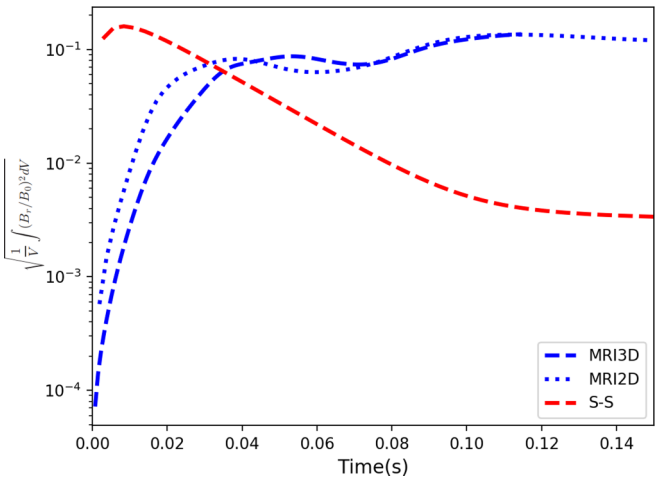

FIG. 11. The evolution of volumetrically averaged B_r (MRI signal) for the MRI unstable and S-S simulations. The MRI signal saturates at a much higher threshold in the MRI unstable configuration compared to the split-stable configuration. Slight differences in the MRI signal evolution for the 2D and 3D cases are due to computational mesh size; the 3D simulations are conducted with a mesh that is four times finer, so the initial perturbation is smaller than the 2D simulations.

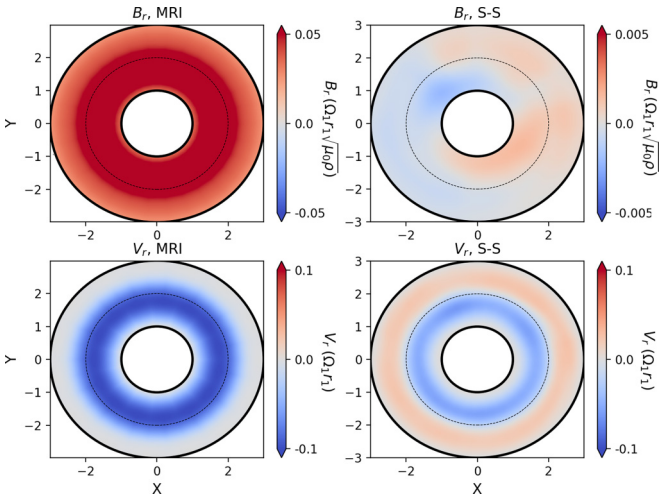

FIG. 13. Azimuthal mode structures of B_r and V_r of the S-S and MRI unstable simulations. Mode structures of V_r are similar in both cases with differences in radial distributions. The azimuthal mode structures of B_r of the MRI unstable configuration and the split-stable configuration are vastly different from each other with a strong dominant axisymmetric $m = 0$ component in the MRI unstable configuration compared to a weak fluctuation in the split-stable configuration.

conducted to compare with the previous two-dimensional (2D) results and the aforementioned split-stable state. Because we expect only the MRI to be unstable in this particular region, the eigenstructures and energy evolution of the MRI unstable configuration should be significantly different from the split-stable configuration, which is shown above to be hydrodynamically unstable.

The volumetrically averaged B_r, called the MRI signal, measures the change in the radial magnetic energy and is plotted for both the split-stable case and the MRI unstable case in Fig. 11. The starting values of the MRI signal are different because the split-stable case is initialized with an experimentally relevant rotation profile with perturbations in V_r, which, in turn, imparts a nontrivial B_r when the background field is turned on. The MRI signal starts near zero for the MRI unstable case because a piecewise solid body initial state was used with no V_r. The saturated value of the MRI signal in the 3D nonaxisymmetric simulations is identical to the 2D simulations, implying that only the axisymmetric $m = 0$ component is present. Furthermore, we can see that, for the MRI unstable case, the MRI signal grows with a saturated state orders of magnitude greater than the counterpart in the split-stable case. This is not surprising because the dominant instability in the split-stable case is hydrodynamically driven, whereas MRI is magnetically driven. Interestingly enough, the

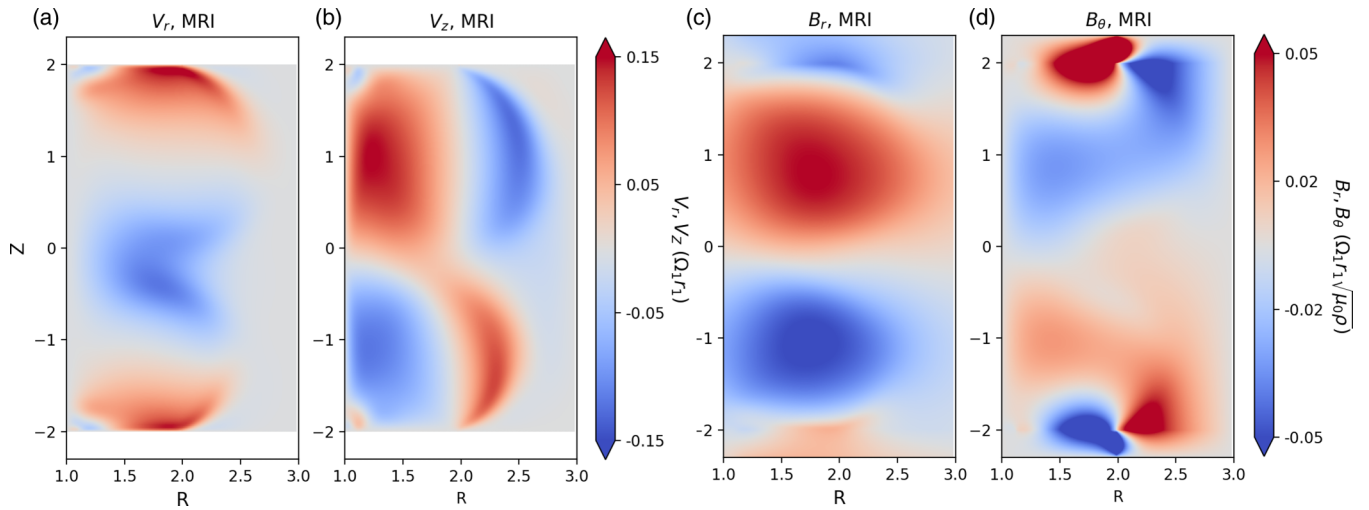

FIG. 12. Axial (r-z) mode structures of (a) V_r, (b) V_z, (c) B_r, and (d) B_θ for the reference MRI unstable simulation. Structures remain axisymmetric even in the presence of nonaxisymmetric modes in the simulations.

MRI signal in the split-stable case exponentially decays and gives rise to hydrodynamic instabilities.

The axial and azimuthal breakdowns of the mode structures of the MRI unstable case also highlight the difference between these two configurations. Figure 12 shows the meridional cross section of B and V for the MRI unstable case. Comparisons with previous 2D results [28] yield identical axial mode structures for the 2D and 3D cases. Comparing the axial structures of the MRI unstable case with the split-stable case (cf. Fig. 7) shows that there is a clear difference in the axial mode structure, indicating that the instability mechanism is different. In particular, the streamlines of V of the split-stable case resemble four vortices whereas, in the MRI unstable case, there are only two vortices on top of each other and spanning the entire radius of the system.

Figure 13 shows the relevant azimuthal mode structures of V_r and B_r of the split-stable configuration and the MRI unstable configuration. The velocity fluctuations are vastly different as expected by the change in parameter space; it is interesting to note that the shear profile of the MRI unstable configuration goes slightly over the centrifugal instability threshold $q = 2$ (cf. Fig. 8). However, the spatial location of the $m = 0$ amplitude in the mode structure of V_r does not overlap with the region of increased shear, suggesting that the centrifugal modes are subdominant. In contrast, B_r has a large active $m = 0$ component orders of magnitude greater than the mostly dormant split-stable counterpart as expected for the axisymmetric MRI perturbations.

IV. CONCLUSION

The effects of boundary end cap conductivity on a free Stewartson-Shercliff in the Princeton MRI experiment were explored using 3D nonaxisymmetric computational simulations. We find that the instabilities resulting from the formation of the free SSLs are global Kelvin-Helmholtz-like modes with insulating axial boundaries, whereas the instabilities resulting from conducting axial boundaries are Rayleigh-like modes. The difference is attributed to the strong coupling of the conducting axial boundary with the working fluid; the immediate evolution of thick boundary layer currents in the end caps leads to return currents in the fluid and stronger coupling, resulting in a strong azimuthal force that ultimately reinforces the flow shear. The increased shear causes the formation of quick Rayleigh modes with finite k_z in the conducting case. In the insulating case, the shear development is too slow to support Rayleigh-like mode growth, thus, the most unstable K-H modes with zero axial wave number ($k_z = 0$) grow.

To summarize, we find that the simulation results with insulating and conducting axial boundaries are consistent with previous experimental measurements [29] using a split-stable rotation profile to enforce large shear in the fluid domain. Our preliminary 3D simulation of the MRI unstable state also shows that there are significant differences in the velocity fluctuations compared to the split-stable case suggesting different instability mechanisms as expected. The magnetic field fluctuations show a strong dominant $m = 0$ component and an increasing MRI signal, which is a promising precursor for MRI.

As experiments and simulations in the MRI unstable regime are carried out, it is important to differentiate between the Rayleigh-like instability and the MRI. Current experimental efforts aim towards minimizing the formation of these SSLs by adjusting the individual rotation rates of the inner and outer rings so that the background hydrodynamic flow becomes flatter to avoid Rayleigh instabilities. Moving forward, it will be important to consider 3D nonaxisymmetric simulations near the stability threshold for experimental relevance and direct comparisons.

ACKNOWLEDGMENTS

This research was supported by the U.S. National Science Foundation (Grant No. AST- 1312463), the U.S. National Aeronautics and Space Administration (Grant No. NNH15AB25I), and the U.S. Department of Energy (Grant No. DE-AC0209CH11466).

[1] N. I. Shakura and R. A. Sunyaev, Astron. Astrophys **24**, 337 (1973).
[2] J. E. Pringle, Annu. Rev. Astron. Astrophys. **19**, 137 (1981).
[3] S. A. Balbus and J. F. Hawley, Rev. Mod. Phys. **70**, 1 (1998).
[4] J. F. Hawley, S. A. Balbus, and W. F. Winters, Astrophys. J. **518**, 394 (1999).
[5] H. Ji, M. Burin, E. Schartman, and J. Goodman, Nature (London) **444**, 343 (2006).
[6] E. M. Edlund and H. Ji, Phys. Rev. E **89**, 021004(R) (2014).
[7] J. Lopez and M. Avila, J. Fluid Mech. **817**, 21 (2017).
[8] R. V. E. Lovelace, H. Li, S. A. Colgate, and A. F. Nelson, Astrophys. J. **513**, 805 (1999).
[9] G. Lesur and J. C. B. Papaloizou, Astron. Astrophys. **513**, A60 (2010).
[10] R. P. Nelson, O. Gressel, and O. M. Umurhan, Mon. Not. R. Astron. Soc. **435**, 2610 (2013).
[11] E. P. Velikhov, Sov. Phys. JETP **36**, 995 (1959).
[12] S. A. Balbus and J. F. Hawley, Astrophys. J. **376**, 214 (1991).
[13] J. Goodman and H. Ji, J. Fluid Mech. **462**, 365 (2002).
[14] G. Rüdiger, M. Schultz, and D. Shalybkov, Phys. Rev. E **67**, 046312 (2003).
[15] A. Kageyama, H. Ji, J. Goodman, F. Chen, and E. Shoshan, J. Phys. Soc. Jpn. **73**, 2424 (2004).
[16] K. Noguchi, I. Pariev, S. Colgate, and J. Nordhaus, Astrophys. J. **575**, 1151 (2002).
[17] D. R. Sisan, N. Mujica, W. A. Tillotson, Y.-M. Huang, W. Dorland, A. B. Hassam, T. M. Antonsen, and D. P. Lathrop, Phys. Rev. Lett. **93**, 114502 (2004).
[18] F. Stefani, T. Gundrum, G. Gerbeth, G. Rüdiger, M. Schultz, J. Szklarski, and R. Hollerbach, Phys. Rev. Lett. **97**, 184502 (2006).
[19] F. Ebrahimi, B. Lefebvre, C. B. Forest, and A. Bhattacharjee, Phys. Plasmas **18**, 062904 (2011).
[20] H. Ji, J. Goodman, and A. Kageyama, Mon. Not. R. Astron. Soc. **325**, L1 (2001).

[21] M. D. Nornberg, H. Ji, E. Schartman, A. Roach, and J. Goodman, Phys. Rev. Lett. **104**, 074501 (2010).
[22] V. W. Ekman, Arch. Math. Astron. Phys. **2**, 1 (1905).
[23] K. Stewartson, J. Fluid Mech. **3**, 17 (1957).
[24] J. Hartmann, Mat. Fys. Medd. **15**, 1 (1937).
[25] J. A. Shercliff, Math. Proc. Cambridge Philos. Soc. **49**, 136 (1953).
[26] C. Gissinger, J. Goodman, and H. Ji, Phys. Fluids **24**, 074109 (2012).
[27] A. H. Roach, E. J. Spence, C. Gissinger, E. M. Edlund, P. Sloboda, J. Goodman, and H. Ji, Phys. Rev. Lett. **108**, 154502 (2012).
[28] X. Wei, H. Ji, J. Goodman, F. Ebrahimi, E. Gilson, F. Jenko, and K. Lackner, Phys. Rev. E **94**, 063107 (2016).
[29] K. J. Caspary, D. Choi, F. Ebrahimi, E. P. Gilson, J. Goodman, and H. Ji, Phys. Rev. E **97**, 063110 (2018).
[30] J. Szklarski, Astron. Nachr. **328**, 499 (2007).
[31] J. Szklarski and G. Gerbeth, Astron. Nachr. **329**, 667 (2008).
[32] F. Stefani, G. Gerbeth, T. Gundrum, R. Hollerbach, J. Priede, G. Rüdiger, and J. Szklarski, Phys. Rev. E **80**, 066303 (2009).
[33] J. L. Guermond, R. Laguerre, J. Leorat, and C. Nore, J. Comput. Phys. **228**, 2739 (2009).
[34] E. Schartman, H. Ji, and M. Burin, Rev. Sci. Instrum. **80**, 024501 (2009).
[35] E. J. Spence, A. H. Roach, E. M. Edlund, P. Sloboda, and H. Ji, Phys. Plasmas **19**, 056502 (2012).
[36] A. Miura and J. R. Kan, Geophys. Res. Lett. **19**, 1611 (1992).